

## ARTICLE OPEN

Momentum-forbidden dark excitons in hBN-encapsulated monolayer MoS<sub>2</sub>Yosuke Uchiyama<sup>1</sup>, Alex Kutana<sup>2</sup>, Kenji Watanabe<sup>3</sup>, Takashi Taniguchi<sup>3</sup>, Kana Kojima<sup>4</sup>, Takahiko Endo<sup>4</sup>, Yasumitsu Miyata<sup>4</sup>, Hisanori Shinohara<sup>1</sup> and Ryo Kitaura<sup>1</sup>

Encapsulation by hexagonal boron nitride (hBN) has been widely used to address intrinsic properties of two-dimensional (2D) materials. The hBN encapsulation, however, can alter properties of 2D materials through interlayer orbital hybridization. In this paper, we present measurements of temperature dependence of photoluminescence intensity from monolayer MoS<sub>2</sub> encapsulated by hBN flakes. The obtained temperature dependence shows an opposite trend to that of previously observed in a monolayer MoS<sub>2</sub> on a SiO<sub>2</sub> substrate. This is caused by the existence of stable momentum-forbidden dark excitons in the hBN-encapsulated MoS<sub>2</sub>. Ab-initio band-structure calculations have shown that orbital hybridization between MoS<sub>2</sub> and hBN leads to upward shift of  $\Gamma$ -valley of MoS<sub>2</sub>, which results in lowering of energy of the momentum-forbidden dark excitons. This work shows an important implication that the hBN-encapsulated structures used to address intrinsic properties of two-dimensional crystals can alter basic properties of encapsulated materials.

npj 2D Materials and Applications (2019)3:26; <https://doi.org/10.1038/s41699-019-0108-4>

## INTRODUCTION

Recently appearing two-dimensional (2D) materials, including graphene, phosphorene, transition metal dichalcogenides (TMDs), etc., have opened up a new field in the science of low-dimensional materials.<sup>1–6</sup> TMDs, in particular, provide a wide variety of 2D layered materials with various compositions and electronic structures, giving us a widespread and excellent field for exploration of physics in the realm of the 2D world. In contrast to graphene, semiconducting 2D-TMDs can have a sizable bandgap up to ~2 eV, which offers an opportunity to explore optical responses at the 2D limit and develop TMD-based nanoelectronic devices.<sup>5,7,8</sup> Furthermore, 2D-TMDs afford vertical or lateral heterostructures, whose electronic structure and physical properties can be tuned through selecting the combination and stacking angles of each layer. Coupled with the possibility arising from the valley degree of freedom,<sup>9,10</sup> TMDs have been yielding new perspectives and attracting a wide range of research interests.

For exploration of the fascinating opportunities, one of the important things is to address intrinsic properties of TMDs. For this purpose, TMDs encapsulated by hexagonal boron nitride (hBN), hBN/TMD/hBN, have been widely used.<sup>11–14</sup> 2D-TMDs are very sensitive to the external environment, such as substrates and adsorbents, because almost all atoms in a 2D-TMD locate at the surface. SiO<sub>2</sub>/Si usually used as a substrate has a rough surface with dangling bonds, low-energy optical phonons, and charged impurities, which can significantly degrade the quality of samples.<sup>15</sup> In contrast, hBN, a graphene analog insulator (bandgap ~6 eV), is free from these degradation factors, providing an ideal environment to address intrinsic properties of 2D-TMDs.

Up to now, quite a few studies have been done with hBN/TMD/hBN to investigate intrinsic properties of 2D-TMDs. For example,

high-mobility devices with hBN-encapsulated structures have been reported, showing carrier mobility of 19–94 cm<sup>2</sup>/V s at room temperature in a monolayer MoS<sub>2</sub> (ML-MoS<sub>2</sub>) encapsulated by hBN flakes; typical mobilities of ML-MoS<sub>2</sub> on silicon substrates range from 1 to 10 cm<sup>2</sup>/V s.<sup>16,17</sup> The enhancement in carrier mobility arises from suppression of the extrinsic carrier scatterings in hBN-encapsulated samples. The high quality of hBN-encapsulated samples has also been observed in optical measurements. Photoluminescence (PL) spectra of an ML-TMD on a silicon substrate show a relatively broad peak arising from radiative recombination of excitons; for example, monolayer WS<sub>2</sub> on a silicon substrate shows a PL peak whose full-width at half-maximum (FWHM) is typically 50–55 or 75 meV. In contrast, the PL spectrum of a hBN/WS<sub>2</sub>/hBN shows a corresponding PL peak with a much smaller FWHM of ~26 meV, and this small FWHM mainly results from suppression of inhomogeneous broadening arising from substrates.<sup>18–20</sup> These results strongly indicate that hBN-encapsulated samples are essential to address intrinsic properties of 2D-TMDs.

In this work, we have focused on the electronic structure of one of the most popular TMDs, ML-MoS<sub>2</sub>, encapsulated by hBN, hBN/MoS<sub>2</sub>/hBN. As discussed above, hBN-encapsulated structures are probably the best structure for investigations of intrinsic properties of TMDs, but a question here is “does the hBN encapsulation really preserve the original electronic structure of a 2D-TMD or not?” In multi-layer systems assembled through van der Waals (vdW) interaction, it has been reported that the band structure of vdW stacks can be modulated by interlayer interaction. Bilayer graphenes are one of the most significant examples. A recent work has revealed that interlayer interaction causes a flat band in a bilayer graphene, which leads to the Mott insulating state and even superconductivity at low temperature.<sup>21,22</sup> Interlayer

<sup>1</sup>Department of Chemistry, Nagoya University, Nagoya 464-8602, Japan; <sup>2</sup>Department of Materials Science and Nanoengineering, Rice University, Houston, TX 77005, USA; <sup>3</sup>National Institute for Materials Science, 1-1 Namiki, Tsukuba 305-0044, Japan and <sup>4</sup>Department of Physics, Tokyo Metropolitan University, Hachioji, Tokyo 192-0397, Japan  
Correspondence: Ryo Kitaura (r.kitaura@nagoya-u.jp)

Received: 18 March 2019 Accepted: 27 June 2019

Published online: 19 July 2019

interaction in hBN/TMD/hBN, at first sight, is not the case, because hBN have a large bandgap of  $\sim 6$  eV and the valence band maximum (VBM) and conduction band minimum (CBM) of TMD locate away from those of hBN, but is this really the case?

In this paper, we show that modification of the band structure of ML-MoS<sub>2</sub> occurs through interlayer interaction between ML-MoS<sub>2</sub> and hBN flakes. Through detailed PL measurements and first-principles band-structure calculations, we have found that the valence band (VB) at the  $\Gamma$ -point of ML-MoS<sub>2</sub> shows upshift due to orbital hybridization, which leads to the existence of stable momentum-forbidden dark excitons. The stable K-K direct exciton is one of the most significant features of ML-MoS<sub>2</sub>; however, in the case of hBN/MoS<sub>2</sub>/hBN, the K-K direct excitons are not the most stable exciton anymore. This band-structure alternation is not sensitive to the relative angle between MoS<sub>2</sub> and hBN, altering significantly optical responses of MoS<sub>2</sub>. This has important implications for investigation of valley-related optical responses at low temperature.

## RESULTS

ML-MoS<sub>2</sub> flakes were grown on exfoliated hBN flakes on a quartz substrate with the chemical vapor deposition (CVD) method using MoO<sub>3</sub> and elemental sulfur as precursors; a high growth

temperature of 1100 °C was applied to improve the crystallinity of grown ML-MoS<sub>2</sub>. A flake of hBN with a thickness of  $\sim 15$  nm was then transferred onto a ML-MoS<sub>2</sub> crystal grown on an hBN flake. After the transfer, the nano-“squeegee” technique<sup>23</sup> was used to remove contaminations encapsulated between the ML-MoS<sub>2</sub> and the hBN flakes. Figure 1 shows an optical microscope image of the ML-MoS<sub>2</sub> encapsulated by hBN flakes. No bubble is visible in the optical image, indicating that the ML-MoS<sub>2</sub> contacts hBN flakes well to form a high-quality hBN-encapsulated structure. An AFM height image of the hBN/MoS<sub>2</sub>/hBN (Fig. 1b) shows an atomically flat surface, giving a height of MoS<sub>2</sub> as  $\sim 0.8$  nm that is consistent with a monolayer structure. The RMS roughness evaluated at the ML-MoS<sub>2</sub> region is  $\sim 0.1$  nm, which clearly demonstrates the atomically flat surface of the prepared sample. This atomically flat structure is essential to suppress inhomogeneous broadening in observations of optical responses.

Figure 2a shows a PL spectrum of the prepared hBN/MoS<sub>2</sub>/hBN measured at 300 K. A single peak arising from radiative recombination of excitons is seen in the PL spectrum, where the contribution from trions is not dominant (a detailed spectral decomposition is shown in Supplementary Fig. 1). The FWHM of the exciton PL peak is 39 meV, which is much smaller than those of samples on silicon substrates (typically  $\sim 70$  or 56 meV).<sup>24,25</sup> Figure 2b shows a PL image of the sample, where the red-dashed

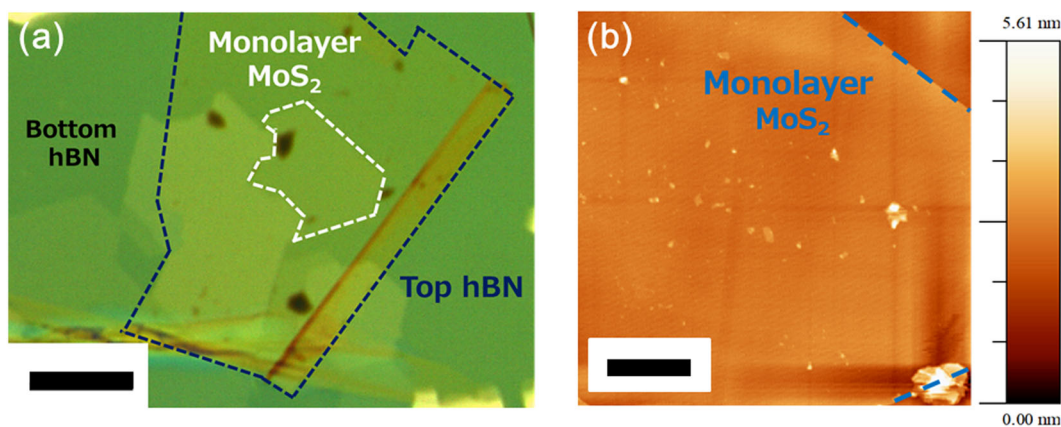


**Fig. 1** Microscopy images of hBN/MoS<sub>2</sub>/hBN. **a** An optical image of the hBN/MoS<sub>2</sub>/hBN prepared. The scale bar corresponds to 10  $\mu$ m. **b** An AFM image of an MoS<sub>2</sub> part in the hBN/MoS<sub>2</sub>/hBN. The scale bar corresponds to 1.5  $\mu$ m

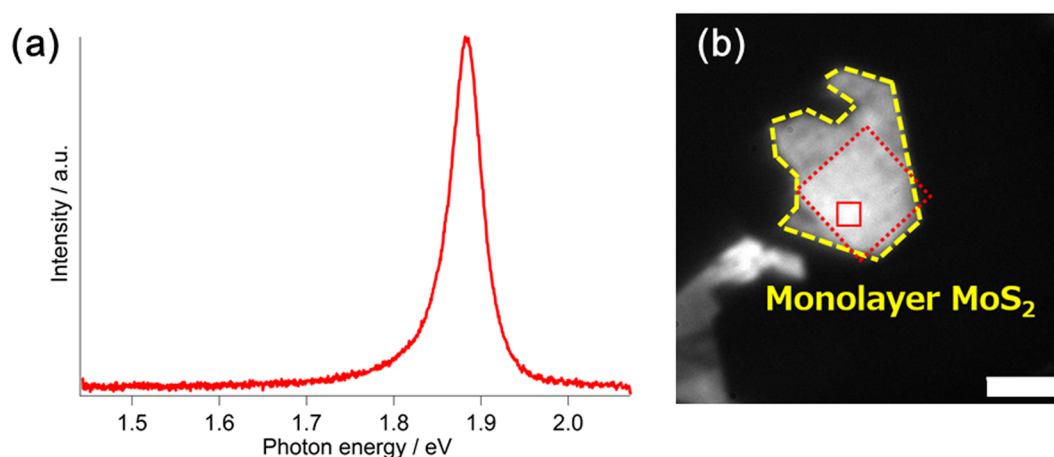


**Fig. 2** A photoluminescence spectrum and image of hBN/MoS<sub>2</sub>/hBN. **a** A photoluminescence spectrum of hBN/MoS<sub>2</sub>/hBN measured at room temperature. Excitation wavelength of 488 nm was used. **b** A photoluminescence image of hBN/MoS<sub>2</sub>/hBN. Bright part corresponds to encapsulated monolayer MoS<sub>2</sub>. The red dotted square shows the place where cleaning with contact-mode AFM was performed. The red square drawn by the solid red line corresponds to the place where integration of PL intensity was performed for evaluation of the temperature dependence of PL intensity. The scale bar corresponds to 5  $\mu$ m

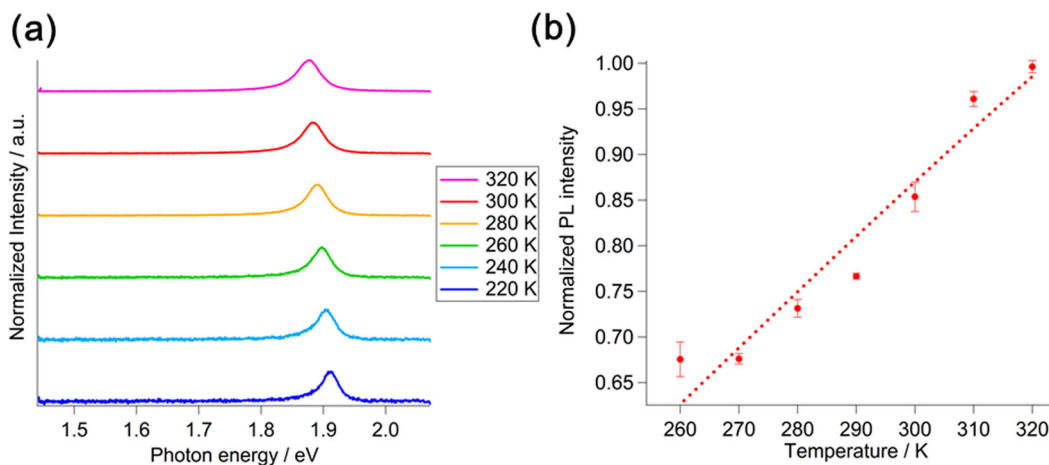


**Fig. 3** Temperature dependence of PL spectra and intensity. **a** Temperature dependence of PL spectra of hBN/MoS<sub>2</sub>/hBN. All measurements were performed with excitation wavelength of 532 nm. All PL spectra are normalized to their maximum PL intensity. **b** Temperature dependence of PL intensity obtained from PL images. The dotted line corresponds to a fitted line with Eq. (1)

rectangle corresponds to the place cleaned by the nano-“squeegee” technique. The PL image, in particular at the red rectangle, clearly shows uniform PL, which represents a high-quality clean interface between ML-MoS<sub>2</sub> and hBN. The brighter PL at the cleaned place indicates that non-radiative decay, which is caused by contaminants, is suppressed.<sup>19,26,27</sup>

Figure 3a shows PL spectra measured at temperatures ranging from 220 to 320 K. PL peaks arising from radiative recombination of excitons show blueshift as temperature decreases, which originates from bandgap widening caused by the electron–phonon interaction. The temperature dependence is well described by Varshni’s equation, which is shown in Supplementary Fig. 2; the obtained parameters are consistent with previously reported values. As you can clearly see, intensities of the PL peaks become weak as temperature decreases. To evaluate the intensity decrease precisely, we measured PL intensity from the red rectangular regions in PL images; PL intensities are averaged over the area to minimize the position-dependent fluctuation. As clearly seen in Fig. 3b, PL intensity monotonically decreases as temperature decreases, and PL intensity at 260 K is two-thirds of that at 320 K.

In a previous report, PL intensity of ML-MoS<sub>2</sub> on a silicon substrate increased as temperature decreased.<sup>28</sup> Ab-initio band-structure calculation tells us that ML-MoS<sub>2</sub> is a direct-gap semiconductor, and bright excitons might be the lowest-energy excited state. This is consistent with the previously reported temperature dependence of PL intensity because the population of bright excitons is expected to increase as temperature decreases if the bright state is the lowest-energy state. A recent theoretical investigation, however, has suggested that lower-energy dark excitons can exist in an ML-MoS<sub>2</sub>, where dark excitons correspond to holes located at the  $\Gamma$ -valley<sup>29</sup>; excitons with  $\Gamma$ -valley holes are dark state because direct recombination is forbidden due to the momentum conservation. The momentum-forbidden dark excitons can have lower energy than K–K direct excitons because of a difference in exciton binding energy. When energy difference between the momentum-forbidden dark excitons and direct excitons is very small, PL intensity in MoS<sub>2</sub>/SiO<sub>2</sub> can still increase as temperature decreases because population of another type of dark excitons, K–K direct excitons with a center-of-mass momentum exceeding the light cone, decreases as temperature decreases.

Figure 4 shows the temperature dependence of time-dependent PL intensity measured with the time-correlated single-photon counting technique. As clearly seen, PL decay becomes faster as temperature becomes lower. Coupled with the

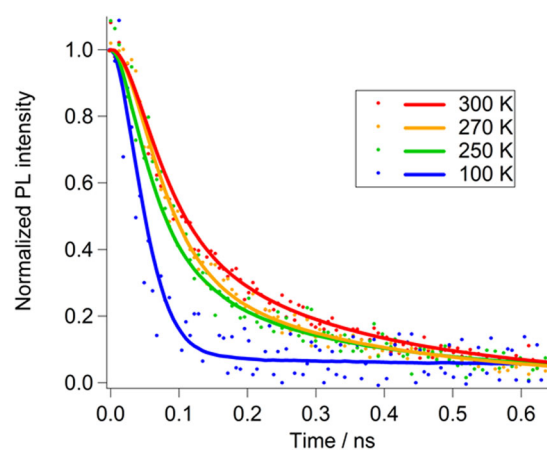


**Fig. 4** Temperature dependence of a time-resolved PL intensity. A time-resolved PL intensity of hBN/MoS<sub>2</sub>/hBN measured with a time-correlated single-photon counting (TCSPC) technique at various temperatures of 100, 250, 270, and 300 K. Dots and solid lines correspond to measured points and fitted curves assuming single exponential decay

observed decrease in PL at low temperature, it is strongly suggested that there is a dark state, whose energy is lower than the bright state, in hBN/MoS<sub>2</sub>/hBN. This dark state should have lower energy than the momentum-forbidden dark states observed in MoS<sub>2</sub>/SiO<sub>2</sub> because temperature dependence in PL intensity of hBN/MoS<sub>2</sub>/hBN is opposite to that of MoS<sub>2</sub>/SiO<sub>2</sub>. To extract the energy difference between bright and dark excitons in the hBN/MoS<sub>2</sub>/hBN, we have fitted the temperature dependence in Fig. 3b with the following equation.

$$I(T) \propto \frac{am_{KK}}{m_{KK} + m_{KK'} + m_{K\Gamma} e^{\beta\Delta E_{K\Gamma}}}. \quad (1)$$

Assuming that PL intensity is proportional to quantum yield, this equation for temperature dependence of PL intensity,  $I(T)$ , can be derived (for details, please see Supplementary Note 1). In this equation, temperature-dependent change in the population of spin-forbidden excitons (K–K’ excitons) and momentum-forbidden dark excitons is considered; there are two kinds of momentum-forbidden dark excitons, inter-valley indirect excitons (K– $\Gamma$  excitons) and direct excitons with momentum exceeding the light cone.  $m_{KK}$ ,  $m_{KK'}$ , and  $m_{K\Gamma}$  in this equation represent exciton

effective masses of K–K bright excitons, K–K' and K– $\Gamma$  dark excitons; effective masses of excitons can be defined by the sum of effective mass of electrons and holes at each valley. In this analysis, we use  $0.835m_e$  for  $m_{KK}$ ,  $m_{KK'}$ , and  $3.175m_e$  for  $m_{K\Gamma}$  based on a previous work.<sup>30</sup>  $\beta$  and  $\Delta E_{K\Gamma}$  in the equation are  $1/k_B T$  ( $k_B$  and  $T$  correspond to the Boltzmann constant and temperature) and the energy difference between K– $\Gamma$  and K–K excitons. As shown by the dashed line in Fig. 3b, the equation reproduces the observed temperature dependence well, giving  $\Delta E_{K\Gamma}$  of 83 meV. This is much larger than the previously reported value for ML-MoS<sub>2</sub> on a silicon substrate, which strongly indicates that the electronic structure is modified in hBN/MoS<sub>2</sub>/hBN.

To address the origin of the dark state in hBN/MoS<sub>2</sub>/hBN, we have performed ab-initio density functional band structure calculations. Figure 5a shows the band structure of isolated ML-MoS<sub>2</sub> and ML-MoS<sub>2</sub> sandwiched by monolayer hBN. Prior to calculation of hBN/MoS<sub>2</sub>/hBN, we performed full structural optimization of isolated ML-MoS<sub>2</sub>, and the optimized structure (optimized primitive vectors and geometry) was used in the calculation of hBN/MoS<sub>2</sub>/hBN; we used a  $4 \times 4$  and  $5 \times 5$  supercells for MoS<sub>2</sub> and hBN to minimize the difference in unit cells. Interlayer distance between MoS<sub>2</sub> and hBN in hBN/MoS<sub>2</sub>/hBN was evaluated with the vdW-DF method (Supplementary Fig. 3). As

you can see, CBM and VBM locate at the K valley in ML-MoS<sub>2</sub>, which is consistent with the band structure previously reported. On the other hand, the VB at the  $\Gamma$ -valley shows upward shift and the VBM locates at the  $\Gamma$ -valley in the hBN/MoS<sub>2</sub>/hBN; i.e. hBN/MoS<sub>2</sub>/hBN is an indirect semiconductor. Because we used the optimized primitive vectors of MoS<sub>2</sub> for the calculation of hBN/MoS<sub>2</sub>/hBN, the observed change in band structure should be caused not by unrealistic strain arising from difference in unit cells but by interlayer interaction between hBN and MoS<sub>2</sub>. The direct-to-indirect change in band structure is consistent with a previous DFT calculation.

This upward shift is very sensitive to interlayer distance between MoS<sub>2</sub> and hBN, showing exponential decay against the interlayer distance (Supplementary Fig. 4). This strong interlayer dependence indicates that the upward shift in the VBM at the  $\Gamma$ -valley originates not from long-range interaction, such as electrostatic interaction, but from orbital hybridization arising from overlap in wave functions between MoS<sub>2</sub> and hBN. It should be noted that accurate estimation of interlayer distance based on DFT is not straight forward and the degree of the upward shift should be influenced by the accuracy. Because the upward shift is caused by orbital hybridization between hBN and MoS<sub>2</sub>, the upward shift should also be sensitive to stacking structure, MoS<sub>2</sub>/

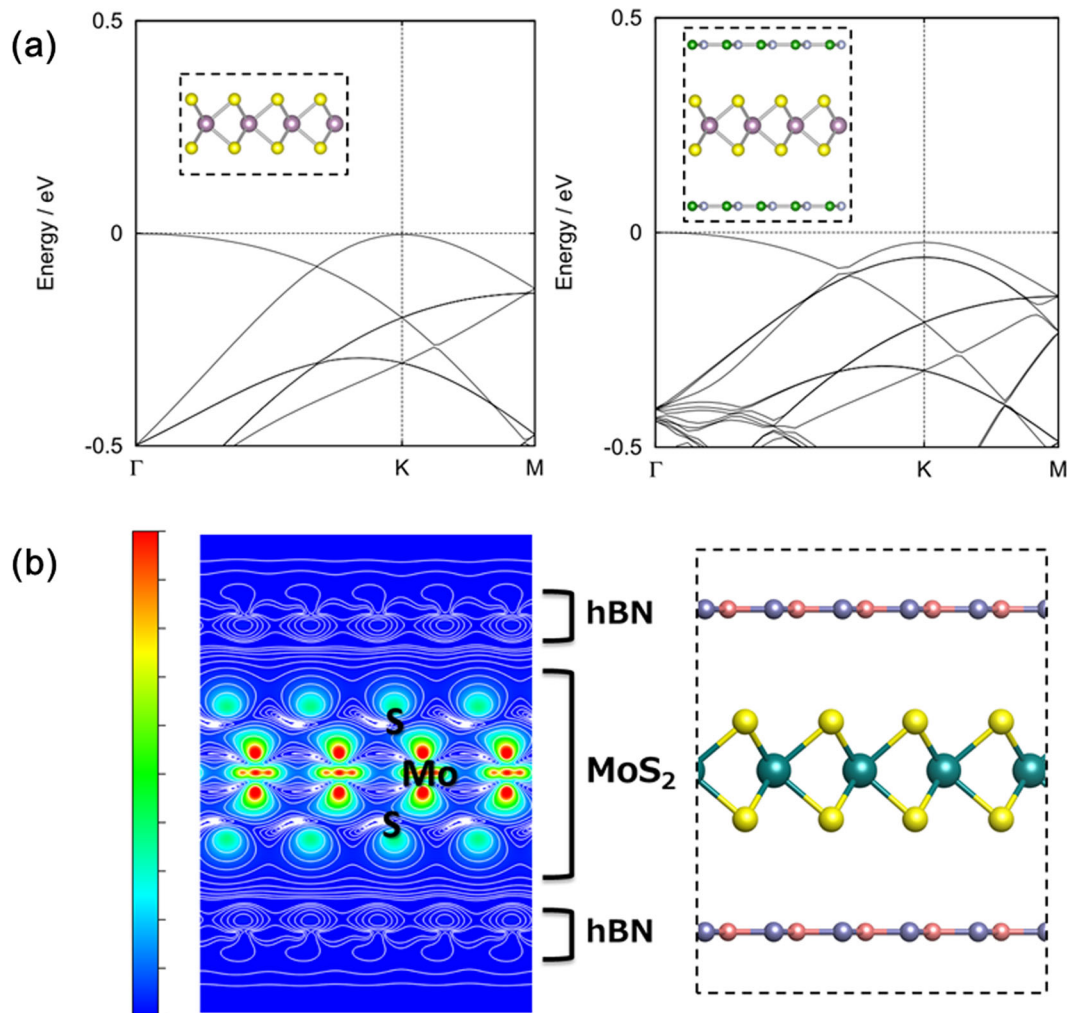


**Fig. 5** Band structures of MoS<sub>2</sub> and hBN/MoS<sub>2</sub>/hBN. **a** Band structures around valence bands of monolayer MoS<sub>2</sub> (left) and hBN/MoS<sub>2</sub>/hBN (right). Insets show structure models used in these calculations, where  $4 \times 4$  and  $5 \times 5$  supercells were used for MoS<sub>2</sub> and hBN, respectively, to minimize the lattice mismatch between MoS<sub>2</sub> and hBN. **b** Cross-section of charge density ( $\psi^2$ ) of hBN/MoS<sub>2</sub>/hBN at the  $\Gamma$ -valley projected along the  $a$ -axis. The contour lines are drawn in such a way that the differences of charge density at adjacent lines are double. All calculations were performed with Quantum Espresso with energy cut-off of 45 Ry and Monkhorst-Pack k-point mesh of  $7 \times 7 \times 1$  were used

hBN and hBN/MoS<sub>2</sub>/hBN. Supplementary Figure 5 shows the PL spectra of MoS<sub>2</sub>/hBN and hBN/MoS<sub>2</sub>/hBN measured at room temperature. As seen in the PL spectra, PL intensity of hBN/MoS<sub>2</sub>/hBN is only half of that of MoS<sub>2</sub>/hBN; we used the same monolayer MoS<sub>2</sub> for both measurements. In the case of MoS<sub>2</sub>/hBN, upward shift of VBM is expected to be smaller than that in hBN/MoS<sub>2</sub>/hBN because the interlayer orbital hybridization, which causes the upward shift of VBM, is less significant in MoS<sub>2</sub>/hBN. The weaker PL intensity observed is consistent with the expected difference in the band structure.

Figure 5b shows a 2D contour plot of the squared wave function of the VBM of hBN/MoS<sub>2</sub>/hBN at the  $\Gamma$ -point; the squared wave function was summed over the  $a$ -axis. As shown in the figure, there is contribution from the  $\pi$ -band of hBN in the wave function of hBN/MoS<sub>2</sub>/hBN. A close inspection has revealed that there is a node between MoS<sub>2</sub> and hBN, and this means that anti-bonding coupling between wavefunctions of MoS<sub>2</sub> and hBN exists in hBN/MoS<sub>2</sub>/hBN. This anti-bonding coupling leads to the upward shift in VBM at the  $\Gamma$ -valley, resulting in the transformation from a direct gap to an indirect gap. The difference in VB energy of hBN and MoS<sub>2</sub> at the  $\Gamma$ -point is  $\sim 400$  meV, which is much smaller than that in CB, and this relatively small energy difference allows the orbital hybridization between hBN and MoS<sub>2</sub>. In addition, there is only a vdW gap between the hBN and MoS<sub>2</sub> layers, and the wave function of MoS<sub>2</sub> at the  $\Gamma$ -point has a significant contribution from sulfur atoms. Both of them contribute to significant spatial overlap between the wave functions of hBN and MoS<sub>2</sub> at the  $\Gamma$ -point, leading to the direct-to-indirect transition.

## DISCUSSION

In contrast to the wavefunction of the VBM at the  $\Gamma$ -point, the wavefunction at the K valley of MoS<sub>2</sub> localizes around molybdenum atoms. This localized nature of the wavefunction plays a major role in small coupling at the K-point; the spatial overlapping between wavefunctions at K-points should be much smaller than that at the  $\Gamma$ -point. In addition, the difference in VB energy between hBN and MoS<sub>2</sub> at the K-point strongly depends on relative angle. The smallest energy difference appears when the relative angle is zero, which is not the case in real samples. Consequently, in real samples, the upward shift of VB energy of MoS<sub>2</sub> at the K-point should be small, which probably contributes to the observed large  $\Delta E_{\text{KG}}$  of 83 meV.

Another scenario that can contribute to the band-structure change is structural distortion. Due to the vdW force acting between the layers, there is a possibility that encapsulated MoS<sub>2</sub> can slightly distort along the direction perpendicular to the 2D plane. The vertical distortion leads to biaxial tensile strain along the direction parallel to the 2D plane, resulting in modification of the band structure (Supplementary Fig. 6). Calculated vertical distortion dependence on the total energy of MoS<sub>2</sub> gives Young's modulus of 225 GPa, which means that 225 MPa is needed to induce 0.1% vertical distortion. Therefore the contribution from distortion cannot be a dominant factor.

In conclusion, we have revealed that the band structure of MoS<sub>2</sub> in hBN/MoS<sub>2</sub>/hBN is significantly altered by interlayer interaction between hBN and MoS<sub>2</sub>. Through detailed PL measurements, including the temperature dependence of PL intensity and time-resolved PL intensity, we have shown the existence of dark excitons, whose energy is 83 meV lower than that of the bright excitons. DFT band structure calculation has revealed that the dark excitons should be momentum-forbidden dark excitons, where electrons and holes locate at the K-point and  $\Gamma$ -point, respectively. The existence of the lower-energy momentum-forbidden excitons in pristine monolayer MoS<sub>2</sub>, originating from the large exciton binding energy, was already pointed out in a previous report. We found, however, that monolayer MoS<sub>2</sub> in hBN/MoS<sub>2</sub>/hBN shows drastically different optical responses due to the orbital

hybridization between MoS<sub>2</sub> and hBN. This should have an impact on valley-related properties of MoS<sub>2</sub>, in particular, properties arising from valley-polarized holes.

## METHODS

### CVD growth of MoS<sub>2</sub> on exfoliated hBN

We have grown monolayer MoS<sub>2</sub> crystals onto hBN flakes by CVD method. We used elemental sulfur (Sigma-Aldrich, 99.98%) and molybdenum oxide (MoO<sub>3</sub>; Sigma-Aldrich, 99.5%) as precursors for the CVD growth. MoO<sub>3</sub>/sulfur was placed in/on a quartz tube with an 8.5 mm inner diameter, and the 8.5 mm inner diameter quartz tube was placed in a 26 mm inner diameter quartz tube to avoid unwanted reaction before reaching the hBN flakes. The hBN flakes were prepared on a quartz substrate by the mechanical exfoliation method, and the quartz substrate with hBN flakes was placed in the downstream of the 8.5 mm diameter quartz tube. The quartz tubes were heated with three-zone furnace at 200°, 750°, and 1100° for 20 min under Ar flow of 200 sccm; sulfur, MoO<sub>3</sub>, and a quartz substrate were placed at the coolest medium and hottest zone, respectively.

### Fabrication of hBN-encapsulated heterostructures

hBN flakes were prepared on an SiO<sub>2</sub>/Si substrate by the mechanical exfoliation method. One of the hBN flakes on an SiO<sub>2</sub>/Si was picked up by a PMMA (Microchem A11)/PDMS (Shin-Etsu Silicone KE-106) film on a glass slide, and the picked-up hBN flake was transferred onto a monolayer MoS<sub>2</sub> grown on an hBN flake to form an hBN/MoS<sub>2</sub>/hBN. To achieve sufficient interlayer contact, we have used the nano-“squeegee” technique, where AFT tip squeezes out contamination and bubbles from interface between hBN and MoS<sub>2</sub>.

### Optical measurements

Room temperature PL spectra were measured by using a confocal Raman microscope (Renishaw InVia Raman and Horiba Jobin Yvon LabRAM HR-800) with 488 nm CW laser excitation (COHERENT Sapphire 488 LP). In measurements of temperature dependence of PL spectra and time-resolved PL measurements, we used a home-built microspectroscopy system equipped with a spectrometer (Princeton Instruments IsoPlane SCT320) and a supercontinuum laser system (NKT Photonics SuperK EXTREME); laser beam from the supercontinuum laser was monochromated by a spectrometer (Princeton Instruments SP2150i). In low-temperature measurements, we placed a sample in a cryostat (CryoVac KONTI-Cryostat-Micro) with continuous flowing of liquid N<sub>2</sub> under vacuum of  $\sim 10^{-4}$  Pa; CryoVac TIC 304-MA was used to control temperature. Objective lenses ( $\times 50$ – $100$  and 0.7–0.85 NA) were used for all measurements.

### First-principles calculations

First-principles density functional theory (DFT) calculations were performed using the Quantum Espresso.<sup>31</sup> Ion–electron interactions were represented by all-electron projector augmented wave potentials,<sup>32</sup> and the generalized gradient approximation (GGA) parameterized by Perdew–Burke–Ernzerhof (PBE)<sup>33</sup> were used to account for the electronic exchange and correlation. The wave functions were expanded in a plane wave basis with energy cut-off of 45 Ry. Prior to band-structure calculation of MoS<sub>2</sub> and hBN/MoS<sub>2</sub>/hBN, the structure of MoS<sub>2</sub> was fully relaxed until the components of Hellmann–Feynman forces on the atoms were less than  $10^{-5}$  Ry/Å. For band-structure calculation, the optimized structure of MoS<sub>2</sub> was expanded to a  $4 \times 4$  supercell to minimize the lattice mismatch between hBN and MoS<sub>2</sub>.

## DATA AVAILABILITY

The authors have confirmed that the data supporting the findings of this study are available within the article and the Supplementary Information. Raw data are available on reasonable requests from the authors.

## ACKNOWLEDGEMENTS

This work was supported by JSPS KAKENHI Grant numbers JP16H06331, JP16H03825, JP16H00963, JP15K13283, JP25107002, and JST CREST Grant Number JPMJCR16F3.

We thank K. Itami and Y. Miyauchi for sharing the Raman and AFM apparatus. We are grateful to S. Okada for fruitful discussion on ab-initio calculation.

## AUTHOR CONTRIBUTIONS

Y.U. prepared hBN/MoS<sub>2</sub>/hBN samples and performed all optical measurements reported in this paper. K.W. and T.T. provided the high-quality single crystalline hBN. K.K., T.E., and Y.M. have contributed to the sample preparation. R.K. performed ab-initio band-structure calculations. Y.U. and A.K. analyzed temperature dependence of PL intensity. R.K. designed the experiments and wrote the manuscript. All authors discussed the results and commented on the manuscript at all stages.

## ADDITIONAL INFORMATION

**Supplementary information** accompanies the paper on the *npj 2D Materials and Applications* website (<https://doi.org/10.1038/s41699-019-0108-4>).

**Competing interests:** The authors declare no competing interests.

**Publisher's note:** Springer Nature remains neutral with regard to jurisdictional claims in published maps and institutional affiliations.

## REFERENCES

- Kitaura, R. et al. Chemical vapor deposition growth of graphene and related materials. *J. Phys. Soc. Jpn* **84**, 121013-1-13 (2015).
- Mak, K. F., Lee, C., Hone, J., Shan, J. & Heinz, T. F. Atomically thin MoS<sub>2</sub>: a new direct-gap semiconductor. *Phys. Rev. Lett.* **105**, 136805-1-4 (2010).
- Novoselov, K. S. et al. Two-dimensional gas of massless Dirac fermions in graphene. *Nature* **438**, 197–200 (2005).
- Li, L. K. et al. Black phosphorus field-effect transistors. *Nat. Nanotechnol.* **9**, 372–377 (2014).
- Wang, Q. H., Kalantar-Zadeh, K., Kis, A., Coleman, J. N. & Strano, M. S. Electronics and optoelectronics of two-dimensional transition metal dichalcogenides. *Nat. Nanotechnol.* **7**, 699–712 (2012).
- Duong, D. L., Yun, S. J. & Lee, Y. H. van der Waals layered materials: opportunities and challenges. *ACS Nano* **11**, 11803–11830 (2017).
- Wang, G. et al. Colloquium: excitons in atomically thin transition metal dichalcogenides. *Rev. Mod. Phys.* **90**, 021001-1-25 (2018).
- Choi, W. et al. Recent development of two-dimensional transition metal dichalcogenides and their applications. *Mater. Today* **20**, 116–130 (2017).
- Xiao, D., Liu, G. B., Feng, W. X., Xu, X. D. & Yao, W. Coupled spin and valley physics in monolayers of MoS<sub>2</sub> and other group-VI dichalcogenides. *Phys. Rev. Lett.* **108**, 196802-1-5 (2012).
- Rivera, P. et al. Interlayer valley excitons in heterobilayers of transition metal dichalcogenides. *Nat. Nanotechnol.* **13**, 1004–1015 (2018).
- Tsen, A. W. et al. Nature of the quantum metal in a two-dimensional crystalline superconductor. *Nat. Phys.* **12**, 208–212 (2016).
- Cui, X. et al. Multi-terminal transport measurements of MoS<sub>2</sub> using a van der Waals heterostructure device platform. *Nat. Nanotechnol.* **10**, 534–540 (2015).
- Wu, S. F. et al. Observation of the quantum spin Hall effect up to 100 kelvin in a monolayer crystal. *Science* **359**, 76–79 (2018).
- Ma, Q. et al. Observation of the nonlinear Hall effect under time-reversal-symmetric conditions. *Nature* **565**, 337–346 (2019).
- Dean, C. R. et al. Boron nitride substrates for high-quality graphene electronics. *Nat. Nanotechnol.* **5**, 722–726 (2010).
- Lee, G. H. et al. Highly stable, dual-gated MoS<sub>2</sub> transistors encapsulated by hexagonal boron nitride with gate-controllable contact, resistance, and threshold voltage. *ACS Nano* **9**, 7019–7026 (2015).
- Yu, H. et al. Precisely aligned monolayer MoS<sub>2</sub> epitaxially grown on h-BN basal plane. *Small* **13**, 1603005 (2017).
- Gutierrez, H. R. et al. Extraordinary room-temperature photoluminescence in triangular WS<sub>2</sub> monolayers. *Nano Lett.* **13**, 3447–3454 (2013).
- Okada, M. et al. Direct chemical vapor deposition growth of WS<sub>2</sub> atomic layers on hexagonal boron nitride. *ACS Nano* **8**, 8273–8277 (2014).
- Zhao, W. J. et al. Evolution of electronic structure in atomically thin sheets of WS<sub>2</sub> and WSe<sub>2</sub>. *ACS Nano* **7**, 791–797 (2013).
- Cao, Y. et al. Unconventional superconductivity in magic-angle graphene superlattices. *Nature* **556**, 43–50 (2018).
- Cao, Y. et al. Correlated insulator behaviour at half-filling in magic-angle graphene superlattices. *Nature* **556**, 80–84 (2018).
- Rosenberger, M. R. et al. Nano-“squeegee” for the creation of clean 2D material interfaces. *ACS Appl. Mater. Interfaces*. **10**, 10379–10387 (2018).
- Kaplan, D. et al. Excitation intensity dependence of photoluminescence from monolayers of MoS<sub>2</sub> and WS<sub>2</sub>/MoS<sub>2</sub> heterostructures. *2D Materials* **3**, 015005–1 (2016).
- Zafar, A. et al. Probing the intrinsic optical quality of CVD grown MoS<sub>2</sub>. *Nano Res.* **10**, 1608–1617 (2017).
- Okada, M. et al. Observation of biexcitonic emission at extremely low power density in tungsten disulfide atomic layers grown on hexagonal boron nitride. *Sci. Rep.* **7**, 322-1-7 (2017).
- Okada, M. et al. Direct and indirect interlayer excitons in a van der Waals heterostructure of hBN/WS<sub>2</sub>/MoS<sub>2</sub>/hBN. *ACS Nano* **12**, 2498–2505 (2018).
- Zhang, X. X., You, Y. M., Zhao, S. Y. F. & Heinz, T. F. Experimental evidence for dark excitons in monolayer WSe<sub>2</sub>. *Phys. Rev. Lett.* **115**, 257403-1-6 (2015).
- Malic, E. et al. Dark excitons in transition metal dichalcogenides. *Phys. Rev. Mater.* **2**, 014002-1-7 (2018).
- Peelaers, H. & Van de Walle, C. G. Effects of strain on band structure and effective masses in MoS<sub>2</sub>. *Phys. Rev. B* **86**, 241401-1-5 (2012).
- Giannozzi, P. et al. QUANTUM ESPRESSO: a modular and open-source software project for quantum simulations of materials. *J. Phys. Condens. Mater.* **21**, 395502-1-19 (2009).
- Bloch, P. E. Projector augmented-wave method. *Phys. Rev. B* **50**, 17953–17979 (1994).
- Perdew, J. P., Burke, K. & Ernzerhof, M. Generalized gradient approximation made simple. *Phys. Rev. Lett.* **78**, 3865–3868 (1997).



**Open Access** This article is licensed under a Creative Commons Attribution 4.0 International License, which permits use, sharing, adaptation, distribution and reproduction in any medium or format, as long as you give appropriate credit to the original author(s) and the source, provide a link to the Creative Commons license, and indicate if changes were made. The images or other third party material in this article are included in the article's Creative Commons license, unless indicated otherwise in a credit line to the material. If material is not included in the article's Creative Commons license and your intended use is not permitted by statutory regulation or exceeds the permitted use, you will need to obtain permission directly from the copyright holder. To view a copy of this license, visit <http://creativecommons.org/licenses/by/4.0/>.

© The Author(s) 2019